

IRAM 30 m LARGE SCALE SURVEY OF $^{12}\text{CO}(2-1)$ AND $^{13}\text{CO}(2-1)$ EMISSION IN THE ORION MOLECULAR CLOUD

O. BERNÉ^{1,2,3}, N. MARCELINO⁴, AND J. CERNICHARO¹

¹ Centro de Astrobiología (CSIC/INTA), Ctra. de Torrejón a Ajalvir, km 4, E-28850, Torrejón de Ardoz, Madrid, Spain; olivier.berne@irap.omp.eu

² Université de Toulouse, UPS-OMP, IRAP, Toulouse, France

³ CNRS, IRAP, 9 Av. colonel Roche, BP 44346, F-31028 Toulouse cedex 4, France

⁴ NRAO, 520 Edgemont Road, Charlottesville, VA 22902, USA

Received 2013 October 22; accepted 2014 August 14; published 2014 October 8

ABSTRACT

Using the IRAM 30 m telescope, we have surveyed a 1×0.8 part of the Orion molecular cloud in the ^{12}CO and $^{13}\text{CO}(2-1)$ lines with a maximal spatial resolution of $\sim 11''$ and spectral resolution of $\sim 0.4 \text{ km s}^{-1}$. The cloud appears filamentary, clumpy, and with a complex kinematical structure. We derive an estimated mass of the cloud of $7700 M_{\odot}$ (half of which is found in regions with visual extinctions A_V below ~ 10) and a dynamical age for the nebula of the order of 0.2 Myr. The energy balance suggests that magnetic fields play an important role in supporting the cloud, at large and small scales. According to our analysis, the turbulent kinetic energy in the molecular gas due to outflows is comparable to turbulent kinetic energy resulting from the interaction of the cloud with the H II region. This latter feedback appears negative, i.e., the triggering of star formation by the H II region is inefficient in Orion. The reduced data as well as additional products such as the column density map are made available online (http://userpages.irap.omp.eu/~oberne/Olivier_Berne/Data).

Key words: infrared: ISM – ISM: lines and bands – ISM: molecules

Online-only material: color figures

1. INTRODUCTION

The structure and dynamical properties of the interstellar medium in galaxies is deeply influenced by the feedback of massive stars. Their ionizing photons (extreme UV, $E > 13.6 \text{ eV}$) generate H II regions, which expand rapidly within their parental molecular cloud. This expansion compresses molecular clouds and can trigger their gravitational collapse toward the formation of a new generation of low-mass stars (Elmegreen 1998; Deharveng et al. 2010). The interaction of the H II region with the surrounding cloud is also a source of hydrodynamical instabilities (Spitzer 1954; Frieman 1954; Berné et al. 2010), turbulence (Elmegreen & Scalo 2004), and chemical mixing (Roy & Kunth 1995; Berné & Matsumoto 2012) in the interstellar medium. In addition, outflows from young stellar objects can also inject kinetic energy into their parent molecular cloud (Bachiller 1996).

Given its proximity to us (414 pc; Menten et al. 2007), the Orion nebula is one of the most studied regions of massive star formation (see, e.g., Genzel & Stutzki 1989; Bally 2008; Muench et al. 2008 for reviews). Traditionally, the “Orion nebula” refers to the visible part of the region, the H II region, powered by the ionizing radiation of the Trapezium OB association. It is part of a much larger complex, referred to as the Orion molecular cloud (OMC), itself lying at the border of the Eridanis super bubble. Numerous studies have focused on specific objects in the Orion nebula, such as the famous Proplyds, the Orion Kleinmann–Low (KL) nebula, or the Orion bar. Studies of the large-scale structure of the nebula are, however, sparse, because of the difficulty to obtain observations covering large areas of the sky with sufficient angular resolution, and because the interpretation of such data sets is challenging. Bally et al. (1987) reported a ^{13}CO observation of the entire Orion molecular cloud, including the nebula, with a resolution of $1'$ (Figure 1). This study was the first to reveal the filamentary structure of the cloud. The Orion nebula was found to lie at the center of an

“integral shaped filament” (ISF) of molecular gas, itself part of a larger filamentary structure extending from north to south over 4° (referred to as Orion A, see Bally et al. 1987 and Figure 1). Several studies have investigated the degree scale properties of the nebula in various molecular tracers. Using ^{12}CO , ^{13}CO , and C^{18}O observations, Castets et al. (1990) provided a column density and an H_2 density map of the ISF with an angular resolution of the order of $100''$. Using C^{18}O observations, Dutrey et al. (1991) identified clumps inside filaments distributed periodically, suggestive of externally triggered cloud collapse and fragmentation. Recently, Buckle et al. (2012) obtained a new survey in $\text{CO}(3-2)$ along the ISF with a $15''$ resolution (see their field of view in Figure 1). Their study concluded that the cloud is magnetically supported and wrapped in a helical magnetic field. Shimajiri et al. (2011) recently reported a survey of the Orion molecular cloud in $\text{CO}(1-0)$ with a spatial resolution of $20''$ and a spectral resolution of 1 km s^{-1} . Using this data set, the authors suggest that the formation of some clumps or protostars might have been triggered by the pressure exerted by the H II region (Shimajiri et al. 2011). The ISF was observed by Johnstone & Bally (1999) in the submillimeter continuum. These authors found a strong correlation between the CO and cold dust continuum emission. They also reported the presence of young stellar objects and prestellar clumps, mainly found in the northern part of the ISF. *Spitzer* observations have shown further evidence for this ongoing low-mass star formation (Megeath et al. 2012). The H II region observed at large scales with VLA at 330 MHz by Subrahmanyam et al. (2001) shows a shell-like structure, suggesting high pressures exerted on the northern cloud, while the gas is escaping in the south toward the general interstellar medium through cavities in the molecular gas. A similar idea was pointed out by Güdel et al. (2008) who have discovered the presence of an X-ray-emitting plasma in thermodynamic equilibrium with the H II gas. Finally, the veil of neutral gas situated in the foreground of the Orion nebula was recently mapped at high angular and spectral resolution by van der Werf et al.

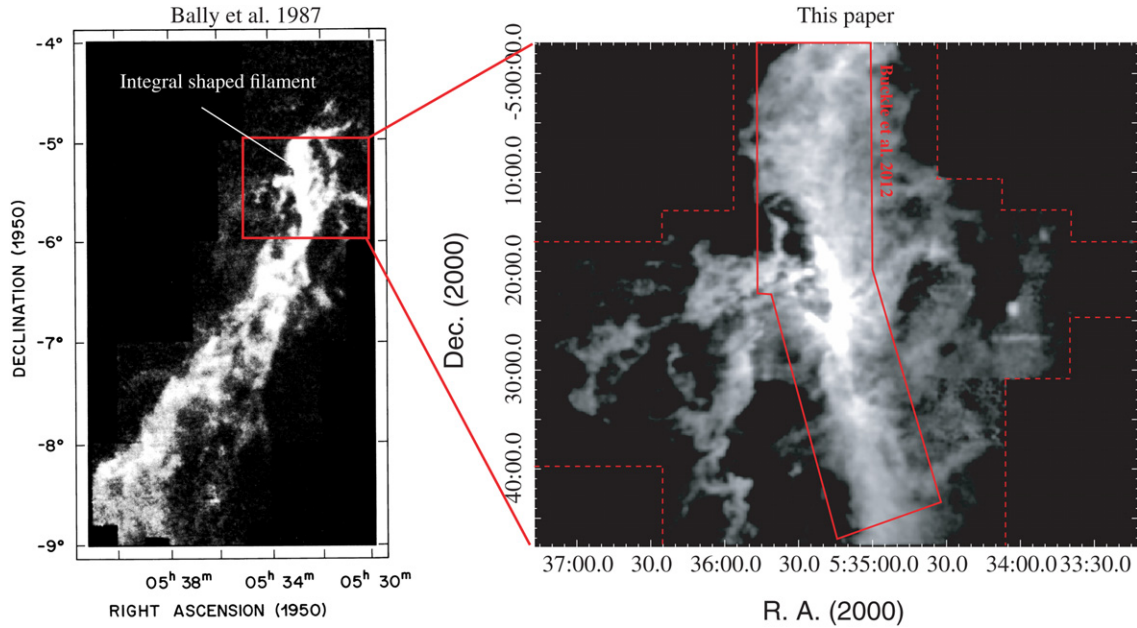


Figure 1. Left: map of the ^{13}CO (1-0) integrated intensity of the Orion A complex presented in Bally et al. (1987) with an angular resolution of $1'$. Right: map of the ^{13}CO (2-1) integrated intensity (see Figure 3 for details) obtained with the IRAM 30 m telescope, with a maximal resolution of $11''$, presented in this article. The limits of the mapped region are indicated with the red dashed line. The polygon with continuous red borders indicates the region mapped in the CO (3-2) line by Buckle et al. (2012). Both maps are shown as gradations of grayscale intensities (see Figure 3 for the absolute scale).

(A color version of this figure is available in the online journal.)

(2013), and seemingly confirms this idea that the H II region is in the blister phase.

In this paper, we present new observations of the ^{12}CO and ^{13}CO (2-1) rotational line at 1.3 mm observed with the IRAM 30 m telescope in Granada. This data set has an unprecedented spatial ($\sim 11''$) and spectral ($\sim 0.4 \text{ km s}^{-1}$) resolution, together with a large field of view (1×0.8). This data are available at http://userpages.iram.omp.eu/~oberne/Olivier_Berne/Data.

2. OBSERVATIONS AND DATA REDUCTION

The observations were conducted at the IRAM 30 m telescope in Granada, Spain, in 2008 March, April, and October. The data were obtained with the HERA receiver array, each polarization tuned to ^{12}CO and ^{13}CO lines (230.5 and 220.4 GHz respectively) with a spatial beamwidth of $11''$, and main beam efficiencies of 0.524 and 0.545 for ^{12}CO and ^{13}CO , respectively. We used the versatile spectrometer VESPA as a backend providing 320 kHz of the spectral resolution, (0.4 km s^{-1}). We observed using the On-The-Fly (OTF) mapping mode, with $5''$ of data sampling in right ascension, and with steps of $12''$ in declination. Since the beam of the telescope is $\sim 11''$, this implies that the resolution is equal to the telescope beam in right ascension, but is a factor of two larger in declination. Intensity calibration was performed every three to four minutes using two absorbers at different temperatures, resulting in system temperatures between 300 and 500 K. Atmospheric opacities were obtained from the measurement of the sky emissivity and the use of the ATM code (Cernicharo 1985; Pardo et al. 2001), and found to be between 0.1 and 0.2 corresponding to 1–3 mm of precipitable water vapor. Focus and pointing were checked every 3 hr and 1.5–2 hr respectively on intense nearby sources. The map is centered at the position of the infrared source IRc2 ($\alpha = 05^{\text{h}}35^{\text{m}}14^{\text{s}}.5$, $\delta = -05^{\circ}22'29''.3$ / $\alpha = 83^{\circ}81'03''.7$, $\delta = -05^{\circ}37'48''.0$). The reference position, which is free of CO emission, was located at an offset ($-3600''$, $-1800''$). Data reduction was per-

formed using the GILDAS software.⁵ Several corrections were applied to the data: one of the problems concerns the combination of submaps obtained over different observing sessions with different intensity calibration, weather conditions, and pointing errors. Position switching observations (PSW) were performed at the position of IRc2 before each OTF submap, and these were used afterwards to correct for such differences between submaps. Relative errors in pointing corrections were obtained comparing these PSW observations with the $4''$ spacing ^{12}CO map observed within the 2×2 line survey (see Esplugues et al. 2013 and Marcelino et al., in preparation). We have found pointing errors between submaps typically of $2\text{--}4''$, with a few cases of large errors of $7\text{--}10''$ in RA under poor weather conditions. Besides the pointing errors in the observations, we found that pixels in the array are not perfectly aligned. We obtained a measurement of pixel misalignment in both HERA1 and HERA2 arrays, using ^{12}CO and ^{13}CO maps of IRC+10216 (Cernicharo et al., in preparation). The errors found are between $0.1\text{--}2''$. Further corrections on the intensity calibration are needed in order to account for the different response of each pixel within the HERA array. The different calibration between pixels is due to the fact that the image band rejection cannot be measured for each individual receiver in the array. Since this parameter will depend on the tuning, maps performed in different days will show different intensity calibrations. Therefore, the data were scaled using a factor that depends on the particular submap and pixel in the array. This factor was obtained comparing the emission in each pixel with respect to the central one in the array, which was found to be the most uniform over the whole map. After all of these corrections were applied, the final map was constructed using a pixel size of $5''.5$, i.e., half the beam size. The total number of positions in the map are 99415 after reduction, each with an on-source integration time of 10 s (~ 1 s at the most

⁵ <http://www.iram.fr/IRAMFR/GILDAS>

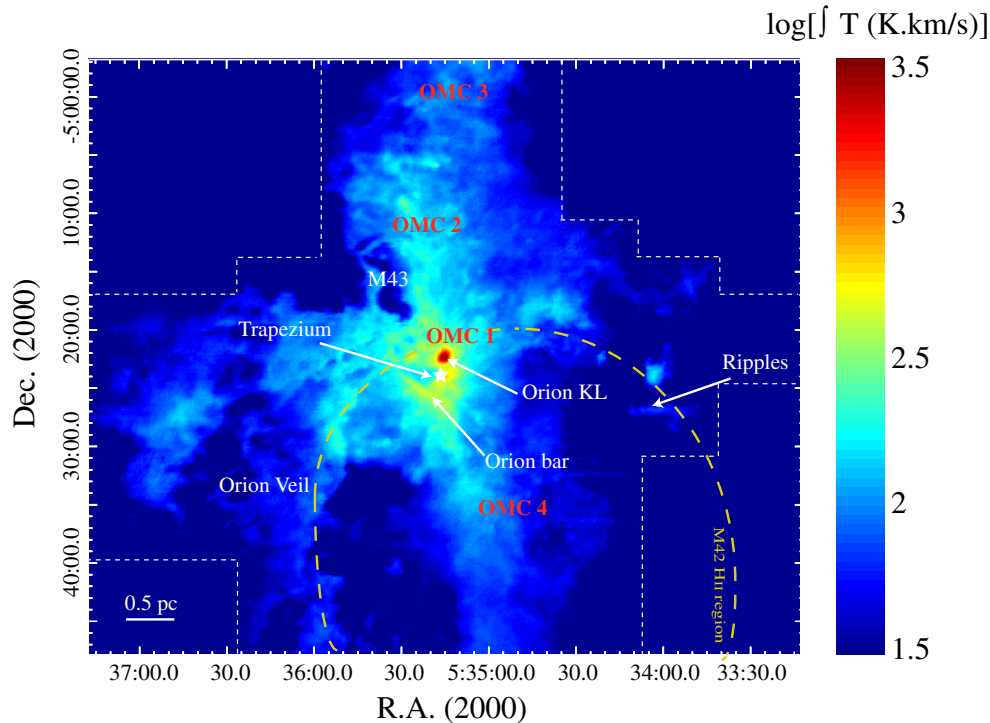


Figure 2. IRAM 30 m maps of the decimal logarithm of velocity integrated ^{12}CO (2-1) emission of the Orion molecular cloud. Distinctive objects within the nebula are indicated. The yellow dashed line indicates the approximate limits of the H II region M42, based on the thermal Bremsstrahlung (free-free) emission observed at 330 MHz by Subrahmanyam et al. (2001), while the white dashed line indicates the limits of the field of view. See http://userpages.iram.omp.eu/~oberne/Olivier_Berne/Data for larger resolution versions of this image and data in FITS format.

(A color version of this figure is available in the online journal.)

external parts of the map) corresponding with an rms of ~ 0.2 K (0.4–0.5 K at the map borders).

3. RESULTS

Figures 2 and 3 show the ^{12}CO and ^{13}CO $J = 2-1$ integrated emission maps between -5 to 25 km s^{-1} . While ^{12}CO shows a widespread emission across the observed region, the less abundant and optically thin isotopomer ^{13}CO , delineates the densest regions, showing a very clumpy and filamentary structure. The bulk of the gas is mainly distributed along the ISF (Bally et al. 1987), clearly delineated by the densest gas seen in ^{13}CO emission (Figure 3). This filament contains the Orion molecular clouds 1–4 (see below). The gas distribution extends east and west of the main filament, but not equally. While emission spreads continuously to the east and southeast, showing numerous clumps and filaments, it is truncated sharply southwest to the filament, coincident with a region where X-ray emission is observed (Güdel et al. 2008). Further west of this empty region where no CO emission was found, a spherical clump and an elongated cloud (E-W) are observed. These features, are only seen at blue shifted velocities (see below), suggesting that they are being pushed toward the observer by a bubble of hot and ionized gas from massive stars. Indeed, the elongated cloud is composed of several clumps (or “ripples”) whose geometry and velocity suggest they are the result of a Kelvin–Helmholtz instability produced by the expansion of the nebula (Berné et al. 2010).

The Orion molecular cloud 1 (OMC-1), located behind the Orion nebula, is the brightest region seen at the center of the filament and contains well-known features such as the BN/KL infrared nebula, the Orion–south region (Ori-S), and the Bar, whose positions are indicated in Figure 2.

In contrast to the bright emission of the Bar, the KL nebula, and Ori-S, there is a small region of weak emission that corresponds to the position of the Trapezium stars. This region is limited by the M42 H II region ionization fronts (the Northern Ionization Front and the Bar to the south), and by the molecular ridge to the west. It is easy to see, in the ^{12}CO maps, the close relation of these bright features with the cone-like ionized structure of M42 observed in the radio-continuum emission (Yusef-Zadeh 1990). The north ionization front (NIF) is formed by several filaments running southwest–southeast (see ^{13}CO emission in Figure 3). The NIF is the counterpart of the obscured filament seen in the optical images of the Orion nebula and known as the “Dark Lane.” Further east, other clumps appear that follow the same direction as the NIF, indicating that they might be related. In ^{12}CO (Figure 2), low density gas east to the NIF is observed. This emission ends abruptly in a wall-like structure from which few thin filaments or streamers spread toward the east, like tunnels blowing the molecular gas to the clumps seen at the easternmost part of the map. South of the NIF, a filamentary structure going nearly north–south is seen (Figure 3), which should also be related to the expansion of the H II region (see Rodriguez-Franco et al. 1998). Cometary shaped pillars are very visible in this region (Figure 3). The fact that these are pointing toward the Trapezium stars strongly suggests that these structures are the result of the selective photo-erosion of the nebula, following the model proposed by Reipurth (1983). This is illustrated in more detail in Figure 4, where we overlay the ^{13}CO emission and the *Spitzer*-IRAC $3.6\mu\text{m}$ image in this particular region. While ^{13}CO traces the inner molecular cloud, the IRAC image is thought to trace the emission from UV heated polycyclic aromatic hydrocarbons (PAHs), present in the mostly atomic gas at the surface of the molecular cloud. It is clear from Figure 4 that the PAH emission

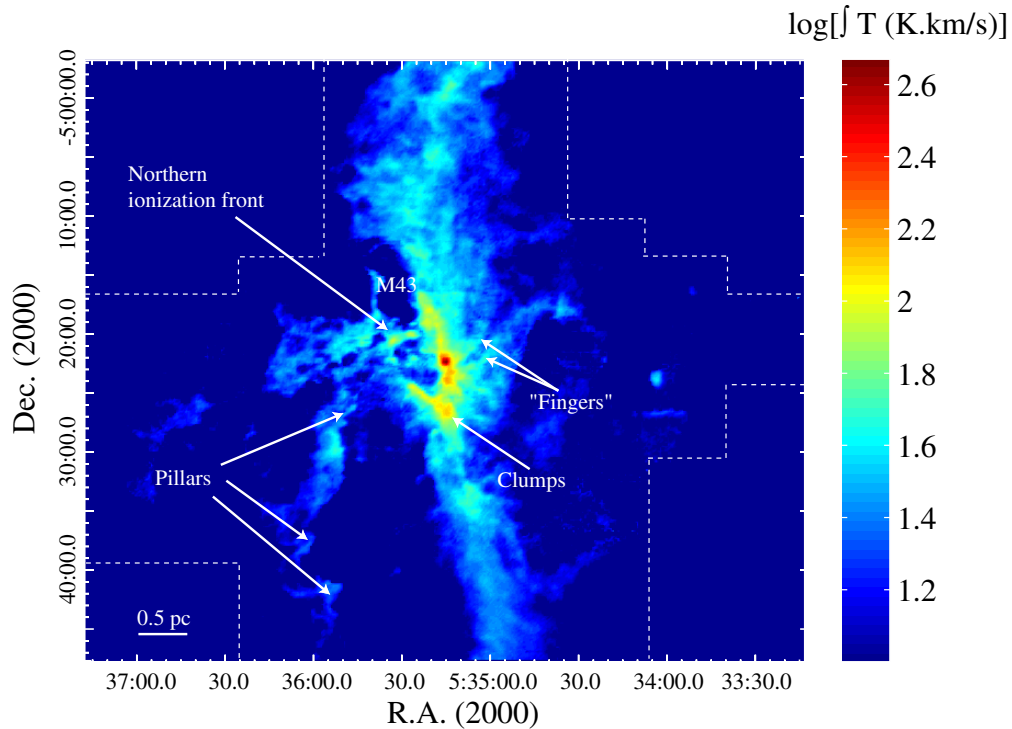


Figure 3. IRAM 30 m maps of the decimal logarithm of velocity integrated ^{13}CO (2–1) emission of the Orion molecular cloud. Distinctive objects within the nebula are indicated. See http://userpages.irap.omp.eu/~oberne/Olivier_Berne/Data for larger resolution versions of this image and data in FITS format.

(A color version of this figure is available in the online journal.)

enshrouds the molecular pillars and peaks systematically closer to the Trapezium stars as compared to CO. This stratification is classical in photon-dominated regions (PDRs, see for instance Tielens et al. 1993 for a classical example in the Orion Bar), and hence also favors the idea that selective photo-erosion is at the origin of these Pillars. Immediately to the west of Orion-KL, elongated structures or *Fingers* (Rodríguez-Franco et al. 1992) are detected. These structures are believed to be the result of the interaction of the molecular cloud with the extreme environment (especially the flow of ionized gas, see discussion in Rodríguez-Franco et al. 1992).

The northern part of the ISF shows strong ^{12}CO emission (Figure 2), which is separated in several clumps in the ^{13}CO map (see Figure 3). This region corresponds to the molecular clouds OMC-2 and OMC-3. Both regions are known to be very active in star formation since many young protostars and premain sequence stars have been detected in the infrared and submillimeter wavelengths, together with molecular outflows and jets (see Peterson & Megeath 2008, for a review). Indeed, the turbulent ^{12}CO emission in OMC-2/3 indicates the presence of such outflows (see Section 4.3). The ^{13}CO emission on the other hand, is very clumpy (Figure 3), showing the densest cores where star formation is taking place. To the southeast of OMC-2, there is a cavity empty of molecular emission, clearly seen in the ^{13}CO map (Figure 3), which corresponds to the H II region M43. This cavity, which in the optical is nearly spherical, is a small H II region illuminated by the B0.5 star ν Ori (Thum et al. 1978). M43 is limited in molecular emission by the ISF to the west, and a thin filament to the east that connects OMC-2 to the NIF. To the south, the ISF seems less clumpy and active in star formation than the northern filament (e.g., no outflow signatures observed). There is a local maximum located about $700''$ south of Orion-KL, corresponding to the OMC-4 molecular cloud. This molecular core was identified in the CO maps of Loren

(1979) and in the SCUBA 450 and $850\ \mu\text{m}$ emission observed by Johnstone & Bally (1999). In their submillimeter maps, this cloud is seen as a bright concentration of knots in a V-shaped structure.

4. ANALYSIS

4.1. Column Density Map

4.1.1. Method

Assuming local thermodynamic equilibrium and optically thin emission (which is mostly the case for ^{13}CO), the ^{13}CO column density can be obtained using an excitation temperature derived from the peak temperature of the ^{12}CO line (see, e.g., Goldsmith & Langer 1999). The ^{13}CO column density can be converted into a column density $N(\text{H}_2)$ using the abundance ratio $[\text{H}_2]/[^{13}\text{CO}] = 7 \times 10^5$. Of course, the derivation of column density in this manner is limited by the assumptions made, in particular, that ^{13}CO may become moderately optically thick in some regions of the nebula with high column densities (see, e.g., Castets et al. 1990). In dense and cold regions, CO is also expected to be depleted on grains and the $[\text{H}_2]/[^{13}\text{CO}]$ ratio may become larger than the one used. Both of these effects will imply an underestimation of the total column density of the order of a few for dense regions. In the rest of the nebula, we expect our estimation to be relatively robust. We have computed N_{H} on each pixel of the map (Figure 5). Column densities derived in this way range between a few times 10^{18} and a few times $10^{23}\ \text{cm}^{-2}$. We have mapped the points that correspond to column densities below $3 \times 10^{21}\ \text{cm}^{-2}$, corresponding to the typical visual extinction at which CO can survive (e.g., Draine 2011). We found that these points correspond to noisy ^{13}CO spectra, i.e., with a peak brightness below 0.6 K, i.e., three times the typical sensitivity of ~ 0.2 K per channel, where the

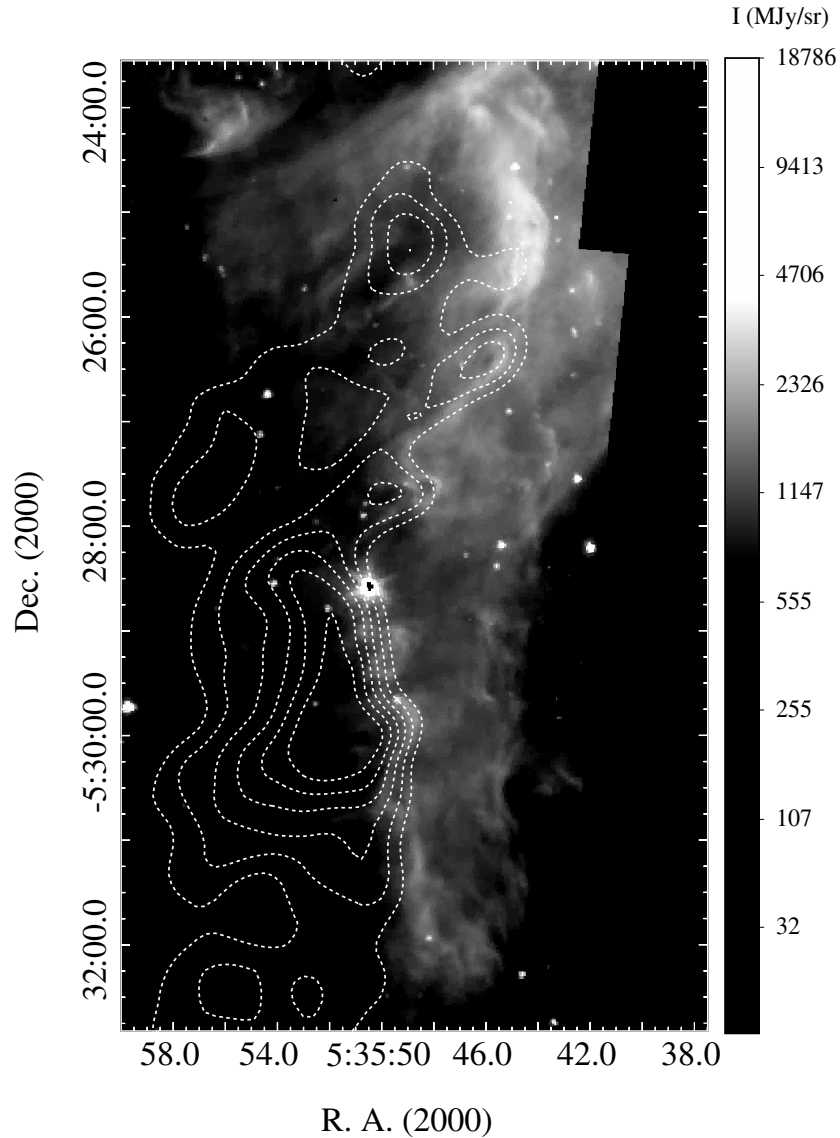


Figure 4. Map of the *Spitzer*–IRAC 3.6 μm emission due to PAHs in the region of the pillars (grayscale). The dashed contours show the velocity integrated ^{13}CO (2–1) intensity. Contours start at 20 K km s $^{-1}$ and increase in steps of 4 K km s $^{-1}$.

column density cannot be evaluated with confidence. Therefore, we have thresholded our map at $3 \times 10^{21} \text{ cm}^{-2}$ (Figure 5). We also arbitrarily define three subregions in the map presented in Figure 5: the north region, which contains OMC-2/3 and corresponds to the regions where many low-mass stars are present, the south region, which contains OMC4, the ripples, and the cometary shaped pillars, and corresponds to the parts of the cloud that enshroud the M42 H II region, and, finally, the central region, corresponding to the most active and complex parts of the nebula, in which Orion-KL, the Bar, the molecular Fingers and the NIF are found.

4.1.2. General Properties

The map of column density derived from the ^{13}CO data is shown in Figure 5. Moderate column densities of a few times 10^{21} – 10^{22} cm^{-2} are found along the ISF. The column density for the Orion-KL is of the order of $5 \times 10^{23} \text{ cm}^{-2}$ (Figure 5) close to the values reported recently by Plume et al. (2012). Figure 6 presents a close-up view of the column density map in the Orion Bar region. The Bar has a typical maximum column density of 10^{23} cm^{-2} . This map suggests the presence of clumpy structures,

and we have identified four specific clumps. They correspond well in position (Table 1) and shape to the clumps seen in the ^{13}CO (3–2) and C^{18}O (3–2) maps of Buckle et al. (2012) (see their Figure 7). The good match between the positions of these clumps in ^{13}CO (2–1), ^{13}CO (3–2), and C^{18}O (3–2) indicates that the emission in these transitions is only moderately affected by optical depth effects in the Bar. We note that these clumps appear relatively large (diameter $> 14''$, see Table 1) and, therefore, differ from the arcsecond scale clumps proposed to exist by van der Werf et al. (1996) and Goicoechea et al. (2011). For the case in which these mini-clumps also exist in the Bar, this would suggest that clumpy structures with different spatial scales coexist. The maximum column densities for these clumps are 9, 10, 11, and $13 \times 10^{22} \text{ cm}^{-2}$ for clumps number 4, 3, 2, and 1 respectively. These values are comparable with the column densities derived for the Orion bar based on far infrared dust emission by Arab et al. (2012). Apart from the ISF and classical structures described above, other notable structures are found with significant column densities: the ripples (a few times 10^{21} cm^{-2}), the clump just north of the ripples (a few times 10^{22} cm^{-2}) as well as the wall of pillars at the edge the

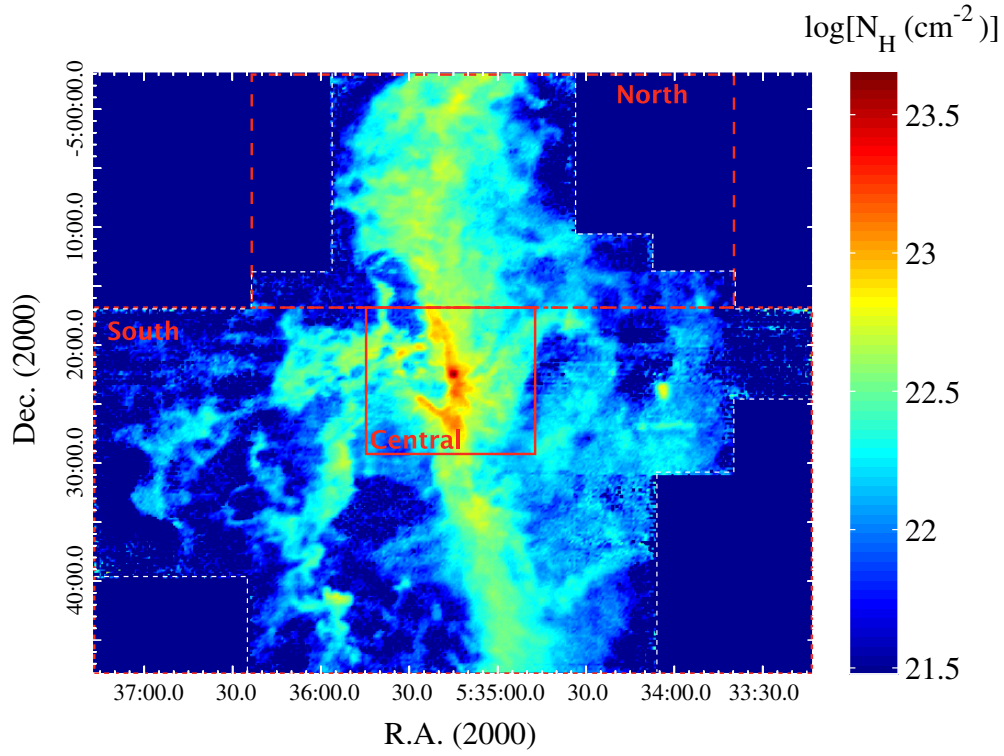


Figure 5. Map of the decimal logarithm of column density N_H in the Orion molecular cloud estimated from the $^{12}\text{CO}(2-1)$ and $^{13}\text{CO}(2-1)$ data (see the text for details). The threshold for this map is $N_H = 3 \times 10^{21} \text{ cm}^{-2}$, corresponding to typical optical depths above which CO is expected to survive to photodissociation. The borders of the subregions mentioned in the text and in Table 2 are indicated with the red dashed boxes. See http://userpages.irap.omp.eu/~oberne/Olivier_Berne/Data for larger resolution versions of this image and data in FITS format.

(A color version of this figure is available in the online journal.)

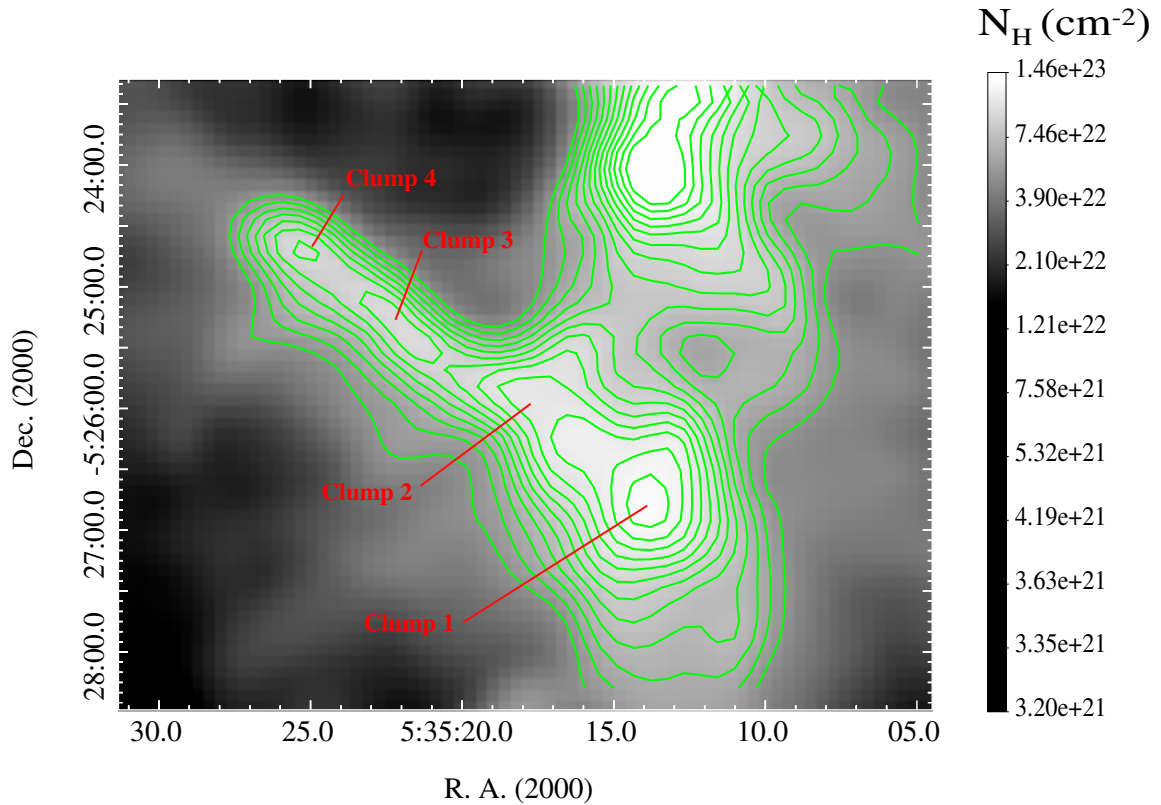


Figure 6. Column density map of the Orion bar region (grayscale). The contours start at $5 \times 10^{22} \text{ cm}^{-2}$ and increase by steps of $2/3 \times 10^{22} \text{ cm}^{-2}$ up to $1.3 \times 10^{23} \text{ cm}^{-2}$. The four clumps identified in the Bar are indicated.

(A color version of this figure is available in the online journal.)

Table 1
Properties of the Clumps in the Orion Bar

Name	Position (R.A., decl.) (deg.)	Radius R_{clump} (")	Mass M_{clump} (M_{\odot})	Velocity Dispersion δV (km s $^{-1}$)	Virial Parameter α
Clump 1	(83.8075, -5.44827)	46.3	52.1	3.03	18.9
Clump 2	(83.8192, -5.43942)	23.4	13.6	2.08	17.3
Clump 3	(83.8431, -5.42102)	23.8	11.3	2.11	21.8
Clump 4	(83.8559, -5.41123)	14.7	4.30	2.12	35.6

Veil in the southeast. The molecular fingers also appear with high column densities (10^{22} – 10^{23} cm $^{-2}$).⁶

4.2. Mass

We can derive the total mass of the cloud using:

$$M = \mu m_H \int_S N(\text{H}_2) dS, \quad (1)$$

where $\mu = 2.8$ is the mean molecular weight and m_H is the atomic hydrogen mass. This integral is calculated on each pixel of the column density map, using the map pixel size ($5'' \times 5''$ at 414 pc) as the unit of surface. The total mass is then derived by summing all the integrals. Using this approach, we find a total mass of $\sim 7700 M_{\odot}$, close to the value derived by Castets et al. (1990) using ^{13}CO (1–0) for a similar field of view. We computed the mass of the integral-shaped filament, using Equation (1), but considering the field of view of Buckle et al. (2012) (see Figure 1). This field is centered on Orion KL and follows the brightest emission of the ISF. With this field of view, we find a mass of $4300 M_{\odot}$, in excellent agreement with the mass of $4290 M_{\odot}$ derived by Buckle et al. (2012) using ^{13}CO (3–2), but smaller than the value reported by Bally et al. (1987) of $5000 M_{\odot}$. Considering that these latter authors used a distance of 500 pc (instead of 414 pc here) and a mean molecular weight of 2.6 (while we use a value of 2.8) to estimate the mass of the ISF, their value could be overestimated by a factor of $(2.6 \times 500^2)/(2.8 \times 414^2) = 1.35$ as compared to ours. On the other hand, in their computation, Bally et al. (1987) consider a north-to-south extent of about $1^{\circ}5$ for the ISF, compared to $0^{\circ}85$ in our case. Overall, we conclude that the mass we derive for the ISF is in very good agreement with the value of Buckle et al. (2012), where a direct comparison is possible. As compared the value of Bally et al. (1987), the agreement is reasonable considering the uncertainty in the area used to derive the mass. Since the total mass we derive for the cloud is about $7700 M_{\odot}$, dense molecular gas present in the ISF actually represents only about half of the cloud mass. Hence, a large fraction of the cloud mass resides in more diffuse extended filamentary structures. Using the column density map, we have estimated that most of this mass in the *diffuse* molecular gas lies in regions of column densities lower than 3×10^{22} cm $^{-2}$, or at a visual extinction A_V below 10. The diffuse and filamentary molecular gas in these regions can be observed thanks to the high sensitivity obtained with the 30 m telescope. These results stress the importance of sensitive surveys in order to calculate accurate masses of molecular gas in nearby and extragalactic environments. Using the same method as above, we derive the masses of the clumps identified in the Orion Bar (see Figure 6). We have assumed a circular geometry with radii given in Table 1. The masses

are found to range between 4.3 and 52 solar masses (Table 1). Condensations with similar masses are often observed around H II regions (see, e.g., Deharveng et al. 2009), and it is believed that they result from the compression of the molecular cloud due to the expansion of the ionized bubble.

4.3. Kinematics

4.3.1. Subtraction of the North–South Velocity Gradient

As mentioned in Bally et al. (1987, see their Figure 5), the Orion A cloud is subject to a velocity gradient over a scale of about 25 pc from north to south. This is also visible at the small scale which we study here, and was reported as well in Buckle et al. (2012) (see their Figure 3 for a position–velocity diagram illustrating this effect). When trying to study the small scale fluctuations of the velocity field, it is, therefore, useful to subtract this velocity gradient. Hence, both our ^{12}CO and ^{13}CO spectral cubes are corrected from a 0.7 km s $^{-1}$ pc $^{-1}$ velocity gradient. This gives spectral cubes that are in the rest frame of the ISF, and can be used to spatially study the fluctuations of the velocity field without contamination from the large-scale *falling backwards* effect. For these two cubes, we redefine $v = 0$ at the peak of the line obtained by averaging the cube over the spatial dimensions.

4.3.2. Kinematics from ^{12}CO

^{12}CO has the advantage of being bright, but, on the other hand, this line quickly becomes optically thick. Hence, it is useful to study detailed spatial structures corresponding to emission in the optically thin high velocity wings of this line. This is particularly suited for the study of outflows and jets emanating from protostars. Using the velocity gradient subtracted cube of ^{12}CO , we compute two maps corresponding to the emission in the high velocity wings of this line. The “blue” map (corresponding to blue shifted velocities in the frame of the ISF) is obtained by integrating the cube in velocity between $[-\infty, -4.8]$ km s $^{-1}$. The “red” map instead is obtained by integrating over the $[+3.2, \infty]$ km s $^{-1}$ range. In Figure 7, we present an overlay of the “blue” and “red” maps. In the south region, OMC-4 appears blue-shifted, most likely because it sits in front of the H II region, and is pushed toward the observer. To the east of OMC-4, an arc-shaped structure is clearly visible. This structure was identified by Loren (1979) and most likely represents the back of the cloud situated behind the H II region. The difference between the mean velocity of the blue- and red-shifted parts of the cloud in the south region is of the order of $\Delta v \sim 10$ km s $^{-1}$. With a radius of 1.8 pc for the H II region, this implies a—short—dynamical age of about $t_{\text{dyn}} \sim 0.2$ Myr for the expansion of the nebula due to the growth of the H II region. The ripples also appear in blue, and hence seem to be part of a foreground cloud as was already proposed by Berné et al. (2010). In the north region, ^{12}CO looks more mixed/turbulent due to red and blue emission most likely arising due to the intense star formation and hence

⁶ The readers interested in the details of the structure of these regions can find the FITS file image of the column density map at http://userpages.irap.omp.eu/~oberne/Olivier_Berne/Data.html.

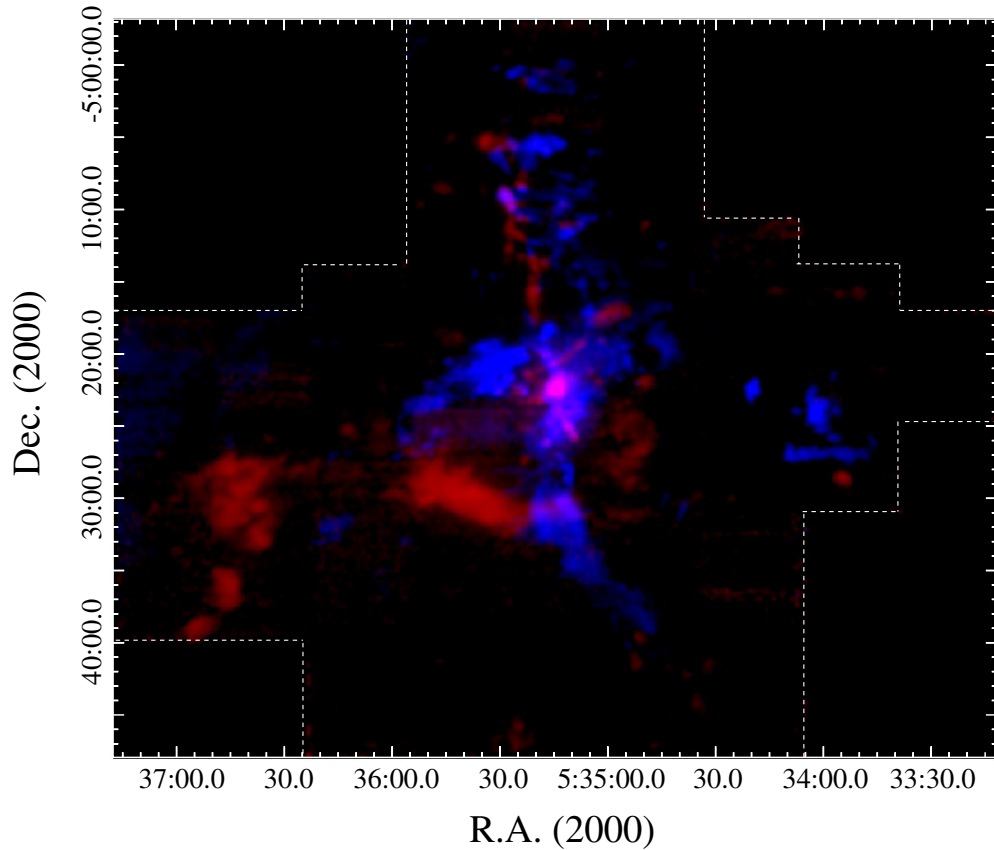


Figure 7. Velocity integrated emission in the wings of the ^{12}CO emission line, after subtraction of the north–south velocity gradient to the spectral cube. Blue corresponds to velocities in the range $[-\infty, -4.8] \text{ km s}^{-1}$ and red corresponds to velocities in the range $[+3.2, \infty] \text{ km s}^{-1}$, where the zero velocity corresponds to the core velocity of the cloud (see the text for details).

(A color version of this figure is available in the online journal.)

outflow activity in this region (e.g., Chini et al. 1997; Aso et al. 2000; Williams et al. 2003). In Figure 8, we overlay the red and blue maps of ^{12}CO to the MIPS $24 \mu\text{m}$ image obtained by *Spitzer*, focusing on the northern region of the nebula only. In addition, we indicate the positions of the far infrared clumpy structures that can be identified (by eye) in the SCUBA $850 \mu\text{m}$ map obtained by Johnstone & Bally (1999). It clearly appears that numerous elongated blue/redshifted structures find their origin at positions of $24 \mu\text{m}$ sources and/or FIR clumps, which are both indicators of the positions of young stellar objects. We do not study these structures individually since this has been done in great detail by Aso et al. (2000) and Williams et al. (2003). Nevertheless, Figure 8 suggests that most of the red and blueshifted structures seen in Figure 8 correspond to protostellar outflows, and that the dynamical properties of the nebula in this region are likely to be affected, or perhaps dominated (Williams et al. 2003), by this activity.

4.3.3. Kinematics from ^{13}CO

As opposed to ^{12}CO , ^{13}CO has the advantage of being more optically thin, but less bright. Hence, it is a useful tracer to study the inner structure of the molecular gas. Using the velocity gradient subtracted cube of ^{13}CO , we compute two maps corresponding to the emission in the blue and redshifted sides of the line, i.e., the “blue” map is obtained by integrating the cube in velocity between $[-\infty, 0] \text{ km s}^{-1}$ and the “red” map instead is obtained by integrating over the $[0, \infty] \text{ km s}^{-1}$ range. In Figure 9, we present an overlay of the corresponding

“blue” and “red” maps. Following the ISF from Orion KL, toward the north or the south, the filament successively appears in red and then blue, with a periodicity of the order of about $20'$. This pattern is compatible with a rotating helical filament, which could be due to the structure of the large-scale magnetic field, which has been suggested to be helical (see Uchida et al. 1991; Matthews et al. 2001; Poidevin et al. 2011; Buckle et al. 2012). Whether this structure is at the origin of the formation of Orion KL (e.g., by the Parker instability as suggested by Shibata & Matsumoto 1991) or resulting from the formation of Orion KL (e.g., acting as a drain of angular momentum as suggested by Uchida et al. 1991) is unclear and should be investigated in more detail. In any case, this suggests that the magnetic field plays a dominant role in the evolution of the cloud. The comparative study between the kinematics of the cloud and the magnetic field combining the present CO data with the large-scale polarization data from the Planck satellite will be particularly useful to investigate this subject.

4.4. Energy Balance

Using the ^{13}CO map, we compute a map of the full width at half maximum (FWHM) of the lines and write this parameter δv . From this, we can derive a map of the turbulent kinetic energy in the gas defined by $E_k = 1/2 M \times \delta v^2$, with M as defined in Equation (1). The total kinetic energy of the cloud is $E_k = 3.6 \times 10^{40} \text{ J}$. This value is slightly higher than the kinetic energy derived by Buckle et al. (2012) of $2.53 \times 10^{40} \text{ J}$, but, as for the mass, this is probably because the field of view

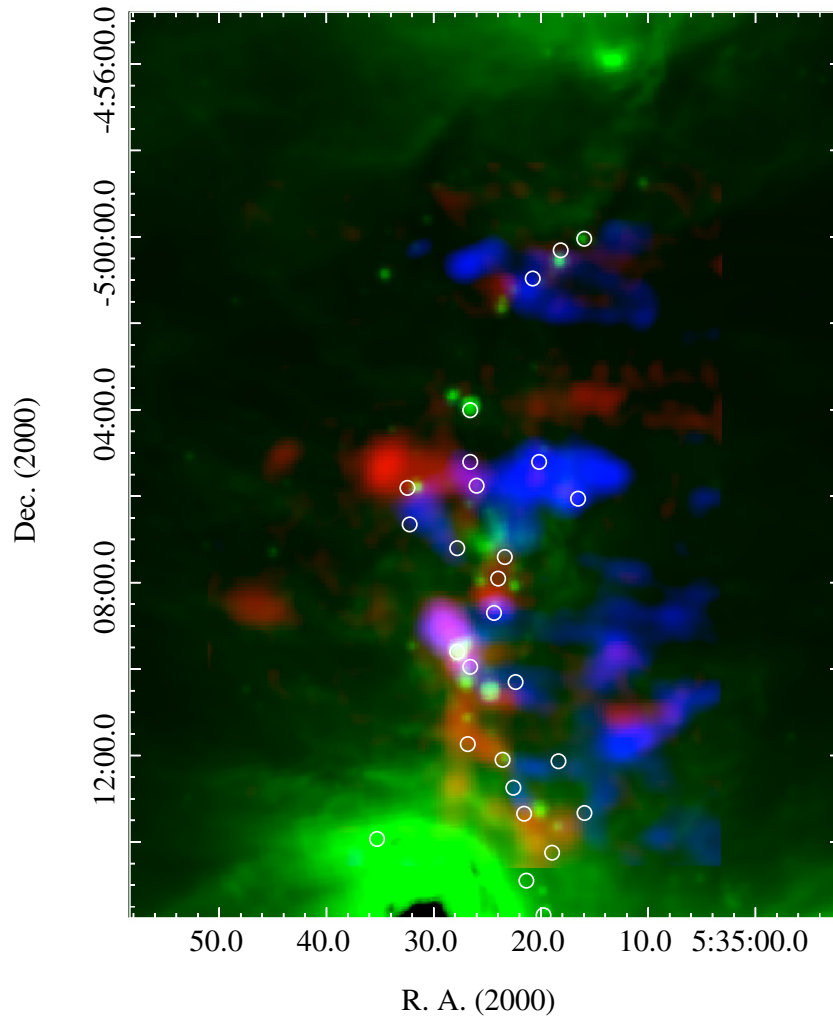


Figure 8. Northern region of the nebula, showing the red and blue components of the ^{12}CO emission (same as those of Figure 7) as well as the *Spitzer*-MIPS $24\,\mu\text{m}$ map in green. The far infrared clumps identified in the SCUBA $850\,\mu\text{m}$ map of Johnstone & Bally (1999) are indicated by the white circles.

(A color version of this figure is available in the online journal.)

studied in the present paper is larger. In the central region, Orion KL contains $\sim 1.1 \times 10^{39}$ J of kinetic energy in the molecular gas. This number is one order of magnitude smaller than that derived by Peng et al. (2012). However, these authors consider the difference between the median velocity in the blue and red wings of the CO (6–5) line to measure velocity dispersion. Therefore, their number is not directly comparable to the one derived here. The Orion Bar contains $\sim 2.3 \times 10^{39}$ J and the molecular fingers $\sim 3.7 \times 10^{39}$ J. The rest of the kinetic energy in the central region is distributed in various filamentary structures, for instance in the northern ionization front filament. The north region holds about 8.9×10^{39} J, a value comparable to the kinetic energy derived by Williams et al. (2003) using CO (1–0) observations of 7.4×10^{39} J, for the same region and attributed to outflows.

Assuming that most of the mass of the nebula lies in the ISF and adopting a cylindrical geometry, we can calculate the gravitational energy by $E_p = 2GM^2/3R$ with R the radius of the cylinder. The CO images suggest a value of $R = 0.2 = 4.2 \times 10^{16}$ m. This yields a gravitational energy $E_p = 2.5 \times 10^{41}$ J, larger than the kinetic energy of the cloud. The thermal energy of the Orion molecular cloud, $E_t = (3/2)k_B T M / \mu m_H = 3.4 \times 10^{39}$ J, is an order of

magnitude smaller than the gravitational potential, adopting a temperature of 50 K for the molecular gas (the molecular gas would need to be 500 K for the thermal energy to be comparable to the gravitational energy, which is unrealistic). The intensity of the magnetic field in the Orion nebula has been measured by Brogan et al. (2005) and Abel et al. (2004) and found to vary between 5 and 25 nT. Adopting a cylindrical geometry once more, we can estimate magnetic energy by $E_B = Rh^2 B/8$, where h is the north-to-south extent of the nebula (measured to be $h = 1.9 \times 10^{17}$ m) and B the magnetic field strength. For the above mentioned values of B , we find a range of magnetic energy $E_B = 2\text{--}10 \times 10^{41}$ J.

In summary, the magnetic energy is comparable to, or larger than, the gravitational potential and an order of magnitude larger than the kinetic energy. The thermal energy in the molecular cloud is negligible compared to these numbers.

Now, focusing on the Orion bar region, we consider the equilibrium for the four clumps seen in the Orion bar (Figure 6). For these four clumps, we derive the mean velocity dispersion $\langle \delta v \rangle$, from the map velocity dispersion δv and inside a circular aperture with position and radii given in Table 2. The values of $\langle \delta v \rangle$ for each clump are given in Table 2. Using the values reported in Table 2 for mass, radius, and velocity

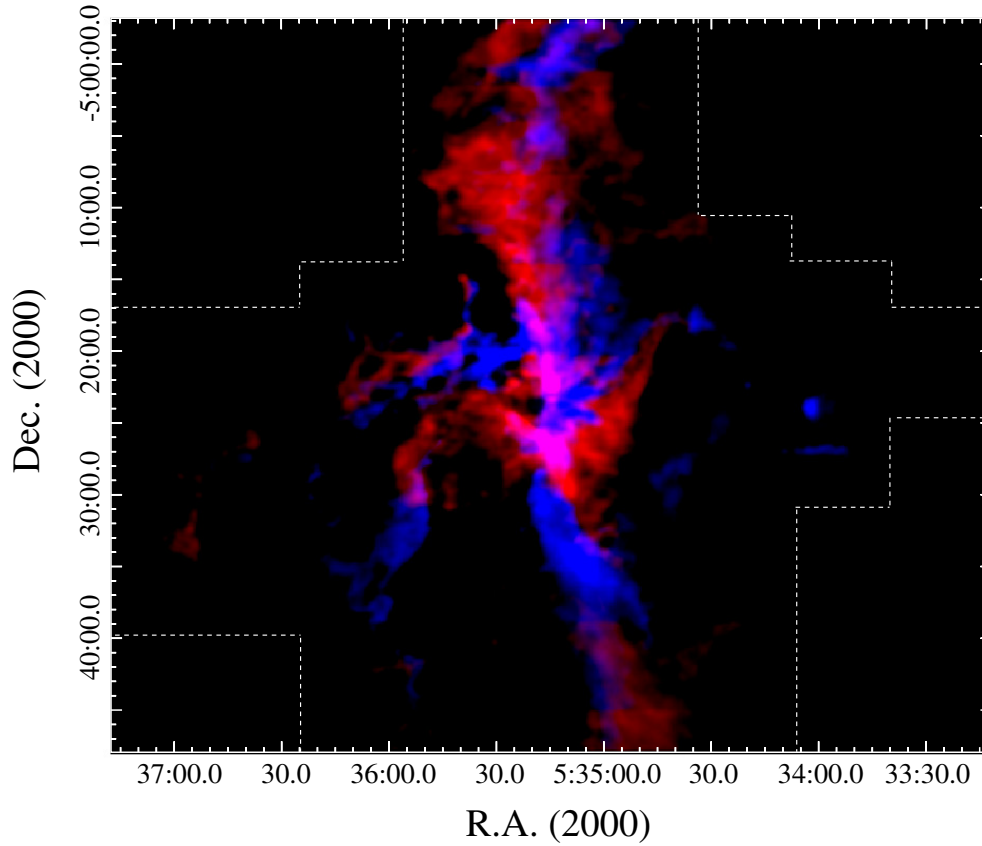


Figure 9. Velocity integrated emission in the ^{13}CO emission line, after the subtraction of the north–south velocity gradient to the spectral cube. Blue corresponds to velocities in the range $[-\infty, 0] \text{ km s}^{-1}$ and red corresponds to velocities in the range $[0, +\infty] \text{ km s}^{-1}$, where the zero velocity corresponds to the core velocity of the cloud (see the text for details).

(A color version of this figure is available in the online journal.)

Table 2
Derived Parameters for the Orion Molecular Cloud

General Parameters	
Total mass, M	$7700 M_{\odot}$
Expansion velocity, ΔV	10 km s^{-1}
Dynamical age, τ_{dyn}	0.2 Myr
Energy (J)	
Turbulent kinetic energy, E_k	3.6×10^{40}
South region (OMC-4)	1.3×10^{40}
North region (OMC 2-3)	8.9×10^{39}
Central region (OMC 1)	1.4×10^{40}
... Orion bar	2.3×10^{39}
... Orion KL	1.1×10^{39}
... Molecular fingers	3.7×10^{39}
... Filamentary structures in the central region	6.5×10^{39}
Gravitational energy, E_p	2.5×10^{41}
Thermal energy, E_t	3.4×10^{39}
Magnetic energy, E_B	$2\text{--}10 \times 10^{41}$
Starlight, E_*	5×10^{44}

dispersion, we can derive the virial parameter defined as (e.g., Bertoldi & McKee 1992) $\alpha = 5\langle\delta v\rangle^2 \times R_{\text{clump}}/GM_{\text{clump}}$ for each clump.

We find that all of the α values are large (Table 2), indicating that these clumps are subcritical and are confined by the external pressure, or are evaporating. Using the physical size (Table 2),

column densities (Figure 6), and a typical gas temperature of 30–50 K yields pressures of the order of a few 10^6 K cm^{-3} for these clumps. Assuming a magnetic field strength of the same order of magnitude as that derived by Abel et al. (2004) (5–25 nT, i.e., 50–250 μG) yields magnetic pressure also of the order of a few 10^6 K cm^{-3} for the ambient medium. Since the magnetic field is expected to increase inside the clump where the density is higher, it will be acting to support the clump against collapse. Thus, the cloud must be evaporating, unless the ambient thermal pressure is greater than a few 10^6 K cm^{-3} . The results of Abel et al. (2004) indicate that the latter is not the case and hence these clumps are probably evaporating. Assuming evaporation at the sound speed yields mass-loss rates lower than a few $10^{-7} M_{\odot} \text{ yr}^{-1}$, these clumps will, therefore, live for timescales larger than that of the nebula.

Overall, this suggests that the magnetic field plays a major role in supporting the integral-shaped filament (Bally et al. 1987; Fiege & Pudritz 2000; Buckle et al. 2012) as well as small-scale structures such as clumps.

4.5. Probability Density Functions

We derive the probability density functions (PDF) of the column density N_{H} , turbulent velocity dispersion δv , and kinetic energy E_k . In addition, we derive the PDF of the turbulent Mach number \mathcal{M} , given by the ratio $\delta v/c_s$, where c_s is the sound speed. c_s is derived assuming that the gas temperature is equal to the excitation temperature derived from the ^{12}CO line. For each one of these parameters, we compute the PDF for the whole

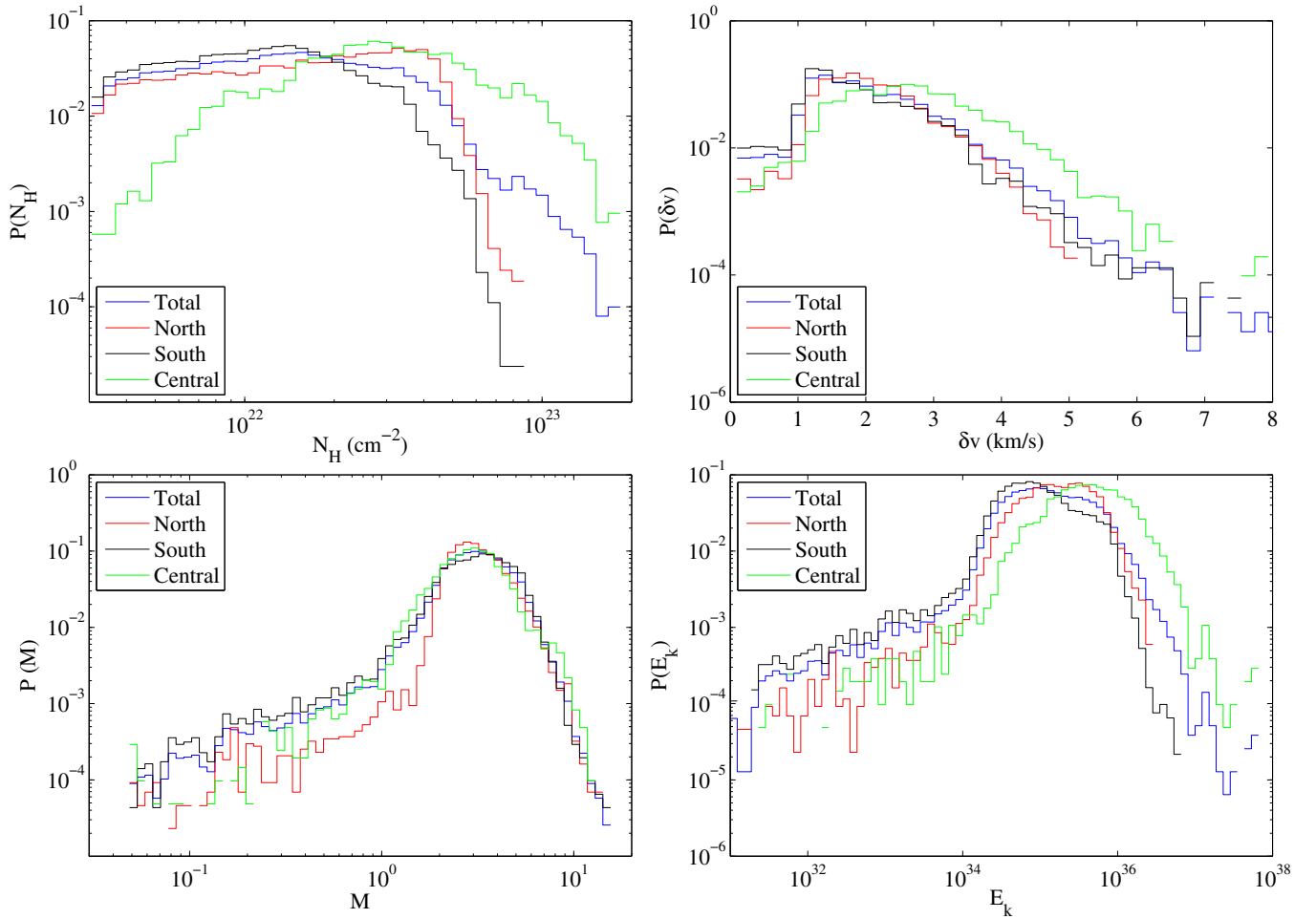


Figure 10. Probability density functions of the per-pixel column density N_H , turbulent velocity dispersion δv , Mach number \mathcal{M} , and kinetic energy E_k . (A color version of this figure is available in the online journal.)

region, but also for the three sub-regions identified in Figure 5. The resulting PDFs are presented in Figure 10.

The column density PDF is found to be non-Gaussian and relatively flat. Column density histograms in star-forming regions are known to exhibit power-law tails (see for instance recent examples in Kainulainen et al. 2011). In our case, the combination of a Gaussian and a power law gives poor fits to the observed histogram. A collection of power laws can give a reasonably good fit, but this is at the expense of many arbitrary choices such as the number of power laws used. It is interesting to note that similarly flat column density PDFs have been produced by MHD simulations of the turbulent saturation of the Kelvin–Helmholtz instability (Hendrix & Keppens 2014), which has been proposed as a source of small-scale turbulence in the Orion molecular cloud by Berné & Matsumoto (2012). When comparing the PDFs of the three subregions, it clearly appears that the central regions host the largest column densities, present in the Orion Bar and Orion-KL. The north region also appears to have higher column densities than the more diffuse south region. The north region shows a sharp decrease at a column density of $N_H \sim 4 \times 10^{22} \text{ cm}^{-2}$, perhaps corresponding to the limit of gravitational stability. Both the higher column density and presence of this sharp edge are consistent with the fact that the north region is much more active in terms of star formation than the south region.

The PDFs of the velocity dispersion show a peak between 1 and 2 km s^{-1} , typical for molecular clouds and a log linear tail

toward larger velocities. The north and south regions show very similar δv PDFs, while the PDF of the central region is shifted toward larger velocities due to the intense kinetic activity of Orion-KL. The PDFs of the Mach number peak around two to three, indicating that turbulence is highly supersonic in Orion. The PDF of the north region appears sharper than in the central and south regions, and peaks at a lower Mach number. This is likely the result of the low-mass star-formation activity, i.e., linked to the fact that turbulence in this region is dominated by the outflow activity.

Finally, the last panel of Figure 10 shows the distribution of the kinetic energy. Logically, the central region contains the pixels with the highest kinetic energies, due to the presence of Orion KL. The north region also displays higher kinetic energies than the south region. This is most likely because of the intense outflow activity in the north region, which can inject kinetic energy efficiently in the molecular cloud.

4.6. Distribution of the Feedback Processes

The distribution of the kinetic energy as well as other sources of energy are summarized in Table 2. In order to estimate the contribution from different feedback processes, we classify the regions and their corresponding kinetic energies either in the “outflow-driven” or “H II region-driven” feedback categories. The kinetic energy in the Orion Bar is most likely the result of the expansion of the H II region and there is very little

outflow activity there. On the contrary, Orion-KL is most likely dominated by outflows, jets, or explosive motions, which all result from the feedback of massive protostars; thus, we classify it in the outflow-driven feedback category. Following Rodríguez-Franco et al. (1992), we consider that the kinetic energy in the molecular fingers results from the interaction of the molecular cloud with the H II region. The situation is less clear for the various filamentary structures seen in the central region. The contribution of both the H II region and outflow may be present; thus, we consider that half of the feedback originates from outflows and the other half from the H II region. In the south region, which is directly in contact with the expanding H II region and where large scale blue and redshifted structures are seen, most of the kinetic energy results from the feedback of the H II region. However, there is known outflow activity in OMC-4, with a kinetic energy of 1.35×10^{39} J (Rodríguez-Franco et al. 1999). In the north, as suggested by Figure 8 and in Section 4.5, the dynamical energy most likely originates largely from outflows of low-mass protostars (see also Williams et al. 2003); thus, we classify this region in the outflow category. All in all, we find that the kinetic energy resulting from outflow activity E_{OF} represents 1.5×10^{40} J while the kinetic energy due to interaction with the H II region E_i represents 2.1×10^{40} J. This implies that 40% of the kinetic energy injected in the cloud is provided by outflows and 60% by the interaction with the H II region.

4.7. Fraction of Radiated Energy Converted into Kinetic Energy

E_i can be compared to the radiative energy injected in terms of ionizing photons by $\theta^1 C$. Assuming that most of its luminosity lies in ionizing photons and using $L_* = 2.1 \times 10^5 L_\odot$, we find $E_* = L_* \times t_{\text{dyn}} \sim 5 \times 10^{44}$ J. Most of this energy is transferred to the H II region (Ferland 2001) in the form of thermal, kinetic, and magnetic energy. With $E_i = 2.1 \times 10^{40}$, this implies that less than $\sim 0.01\%$ of the energy injected in starlight has been transferred in the molecular cloud in the form of kinetic energy. This value is naturally small, because most of the energy of the H II region is radiated away. An additional fraction of kinetic energy may be present in the H II region (photo-evaporation flows, champagne flows; see, e.g., Ochsendorf et al. 2014) but this has not been evaluated observationally thus far. Assuming a total lifetime for $\theta^1 C$ of ~ 3 Myr and a constant injection efficiency implies that, in total, a few times 10^{41} J of kinetic energy will be injected in the ISM due to the evolving H II region. This is at least one order of magnitude smaller than what can be injected by a supernova explosion (Thornton et al. 1998), but is distributed over a much longer timescale, and may thus have a profound impact on the evolution of the galactic ecosystem and on triggered star formation.

4.8. On Triggered Star Formation in Orion

Triggered star formation theories stipulate that the formation of a massive star and the following expansion of an H II region can compress and fragment the surrounding molecular cloud, resulting in the formation of a subsequent generation of low-mass stars. This process has been convincingly identified to be at play in the molecular shells around a number of bubble shaped H II regions (see, e.g., Deharveng et al. 2010 for a recent overview). Here, on the other hand, we find that the molecular cloud directly in contact with the H II region in the south (OMC4, the Veil) shows lower column densities than the northern region

(OMC 2-3). Such conditions disfavor star formation, and indeed the south region shows very few signs of star-forming activity, though Shimajiri et al. (2011) have identified a few subregions where star formation could occur. Clearly, the north region contains much more protostars than the south region, and this suggests that the triggered star formation due to the H II region is not effective in Orion. Given the young dynamical age we have derived (0.2 Myr), it is possible that triggering will occur later. Alternatively, an explanation could be that triggered star formation at the edge of expanding H II regions is only favored around well-confined H II bubbles. Here, in Orion, instead, the H II region may not be well-confined and a champagne flow could be releasing the pressure, especially through a cavity toward the Eridanis super-bubble in the southeast (Güdel et al. 2008). In this case, the Orion H II region would already be in the blister phase, and, therefore, the pressure-driven expansion of the H II region is expected to be much reduced, as well as the compression of the surrounding cloud and the triggering of star formation.

5. SUMMARY AND CONCLUSIONS

We presented new large-scale maps of the Orion molecular cloud in the ^{12}CO and ^{13}CO (2–1) lines. The nebula appears filamentary and turbulent. Using this data set we derive the following parameters: a dynamical age for the nebula $t_{\text{dyn}} \sim 0.2$ Myr and a total mass of the nebula $M = 7700 M_\odot$. About half of this mass resides in the dense integral-shaped filament at the center of the nebula, while the other half resides in more diffuse and filamentary structures distributed around the filament. We find a total kinetic energy $E_k = 3.6 \times 10^{40}$ J for the cloud, about 40% of which emanates from the outflows and the rest from feedback of the H II region. However, the relative importance of the feedback processes depends on the considered subregions within the cloud. The north region of the cloud, (OMC-2/3) seems to be dominated by feedback from outflows. In the central region (OMC-1), the feedback is shared between the protostellar outflows and feedback from the H II region. The south region, instead, seems dominated by the feedback due to the expansion of the H II region. Overall, it seems that the feedback from the H II region, which is often invoked as a major trigger of star formation, is not significantly larger than the feedback from outflows, and, therefore, both mechanisms may be important. In addition, we find that the triggering of star formation by the expansion of the H II region seems inefficient in Orion. We find that only about $\sim 0.01\%$ of the energy radiated by $\theta^1 C$ has been converted into kinetic energy in the molecular cloud. Over the lifetime of this star, a few 10^{41} J may be injected in the ISM. This is much smaller than what can be injected by a supernova but can still have a significant influence on the shaping of the ISM and the regulation of star formation, since this occurs on larger timescales. Finally, we suggest that magnetic fields probably play an important role in the energy balance at both small and large scales. We propose that the integral shaped filament has a helical shape, perhaps following the magnetic field lines and is rotating about its main axis.

We acknowledge the two referees of this paper who helped improve the manuscript. We thank Paul Goldsmith for his comments. The National Radio Astronomy Observatory is a facility of the National Science Foundation operated under cooperative agreement by Associated Universities, Inc.

REFERENCES

- Abel, N. P., Brogan, C. L., Ferland, G. J., et al. 2004, *ApJ*, **609**, 247
- Arab, H., Abergel, A., Habart, E., et al. 2012, *A&A*, **541**, A19
- Aso, Y., Tatematsu, K., Sekimoto, Y., et al. 2000, *ApJS*, **131**, 465
- Bachiller, R. 1996, *ARA&A*, **34**, 111
- Bally, J. 2008, in *Handbook of Star Forming Regions*, ed. B. Reipurth (San Francisco, CA: ASP), 459
- Bally, J., Lanber, W. D., Stark, A. A., & Wilson, R. W. 1987, *ApJL*, **312**, L45
- Berné, O., Marcelino, N., & Cernicharo, J. 2010, *Natur*, **466**, 947
- Berné, O., & Matsumoto, Y. 2012, *ApJL*, **761**, L4
- Bertoldi, F., & McKee, C. F. 1992, *ApJ*, **395**, 140
- Brogan, C. L., Troland, T. H., Abel, N. P., Goss, W. M., & Crutcher, R. M. 2005, in *ASP Conf. Ser. 343, Astronomical Polarimetry: Current Status and Future Directions*, ed. A. Adamson, C. Aspin, C. Davis, & T. Fujiyoshi (San Francisco, CA: ASP), 183
- Buckle, J. V., Davis, C. J., Francesco, J. D., et al. 2012, *MNRAS*, **422**, 521
- Castets, A., Duvert, G., Dutrey, A., et al. 1990, *A&A*, **234**, 469
- Cernicharo, J. 1985, *IRAM Report Number 52*
- Chini, R., Reipurth, B., Ward-Thompson, D., et al. 1997, *ApJL*, **474**, L135
- Deharveng, L., Schuller, F., Anderson, L. D., et al. 2010, *A&A*, **523**, A6
- Deharveng, L., Zavagno, A., Schuller, F., et al. 2009, *A&A*, **496**, 177
- Draine, B. T. 2011, *Physics of the Interstellar and Intergalactic Medium* (Princeton, NJ: Princeton Univ. Press)
- Dutrey, A., Duvert, G., Castets, A., et al. 1991, *A&A*, **247**, L9
- Elmegreen, B. G. 1998, in *ASP Conf. Ser. 148, Origins*, ed. C. E. Woodward, J. M. Shull, & Jr. H. A. Thronson (San Francisco, CA: ASP), 150
- Elmegreen, B. G., & Scalo, J. 2004, *ARA&A*, **42**, 211
- Esplugues, G. B., Tercero, B., Cernicharo, J., et al. 2013, *A&A*, **556**, A143
- Ferland, G. J. 2001, *PASP*, **113**, 41
- Fiege, J. D., & Pudritz, R. E. 2000, *ApJ*, **534**, 291
- Frieman, E. A. 1954, *ApJ*, **120**, 18
- Genzel, R., & Stutzki, J. 1989, *ARA&A*, **27**, 41
- Goicoechea, J. R., Joblin, C., Contursi, A., et al. 2011, *A&A*, **530**, L16
- Goldsmith, P. F., & Langer, W. D. 1999, *ApJ*, **517**, 209
- Güdel, M., Briggs, K. R., Montmerle, T., et al. 2008, *Sci*, **319**, 309
- Hendrix, T., & Keppens, R. 2014, *A&A*, **562**, A114
- Johnstone, D., & Bally, J. 1999, *ApJL*, **510**, L49
- Kainulainen, J., Beuther, H., Banerjee, R., Federrath, C., & Henning, T. 2011, *A&A*, **530**, A64
- Loren, R. B. 1979, *ApJL*, **234**, L207
- Matthews, B. C., Wilson, C. D., & Fiege, J. D. 2001, *ApJ*, **562**, 400
- Megeath, S. T., Gutermuth, R., Muzerolle, J., et al. 2012, *AJ*, **144**, 192
- Menten, K. M., Reid, M. J., Forbrich, J., & Brunthaler, A. 2007, *A&A*, **474**, 515
- Muench, A., Getman, K., Hillenbrand, L., & Preibisch, T. 2008, in *Handbook of Star Forming Regions*, Vol. I, ed. B. Reipurth (San Francisco, CA: ASP), 483
- Ochsendorf, B. B., Verdolini, S., Cox, N. L. J., et al. 2014, *A&A*, **566**, 75
- Pardo, J., Cernicharo, J., & Serabyn, E. 2001, *ITAP*, **49**, 1683
- Peng, T.-C., Zapata, L. A., Wyrowski, F., Güsten, R., & Menten, K. M. 2012, *A&A*, **544**, L19
- Peterson, D. E., & Megeath, S. T. 2008, in *Handbook of Star Forming Regions*, ed. B. Reipurth (San Francisco, CA: ASP), 590
- Plume, R., Bergin, E. A., Phillips, T. G., et al. 2012, *ApJ*, **744**, 28
- Poidevin, F., Bastien, P., & Jones, T. J. 2011, *ApJ*, **741**, 112
- Reipurth, B. 1983, *A&A*, **117**, 183
- Rodríguez-Franco, A., Martín-Pintado, J., & Fuente, A. 1998, *A&A*, **329**, 1097
- Rodríguez-Franco, A., Martín-Pintado, J., Gómez-González, J., & Planesas, P. 1992, *A&A*, **264**, 592
- Rodríguez-Franco, A., Martín-Pintado, J., & Wilson, T. L. 1999, *A&A*, **351**, 1103
- Roy, J.-R., & Kunth, D. 1995, *A&A*, **294**, 432
- Shibata, K., & Matsumoto, R. 1991, *Natur*, **353**, 633
- Shimajiri, Y., Kawabe, R., Takakuwa, S., et al. 2011, *PASJ*, **63**, 105
- Spitzer, L., Jr. 1954, *ApJ*, **120**, 1
- Subrahmanyan, R., Goss, W. M., & Malin, D. F. 2001, *AJ*, **121**, 399
- Thornton, K., Gaudlitz, M., Janka, H.-T., & Steinmetz, M. 1998, *ApJ*, **500**, 95
- Thum, C., Lemke, D., Fahrback, U., & Frey, A. 1978, *A&A*, **65**, 207
- Tielens, A. G. G. M., Meixner, M. M., van der Werf, P. P., et al. 1993, *Sci*, **262**, 86
- Uchida, Y., Fukui, Y., Minoshima, Y., Mizuno, A., & Iwata, T. 1991, *Natur*, **349**, 140
- van der Werf, P. P., Goss, W. M., & O'Dell, C. R. 2013, *ApJ*, **762**, 101
- van der Werf, P. P., Stutzki, J., Sternberg, A., & Krabbe, A. 1996, *A&A*, **313**, 633
- Williams, J. P., Plambeck, R. L., & Heyer, M. H. 2003, *ApJ*, **591**, 1025
- Yusef-Zadeh, F. 1990, *ApJL*, **361**, L19